

Synchronization of Micromechanical Oscillators Using Light

Mian Zhang*,¹ Gustavo Wiederhecker*,^{1,2} Sasikanth Manipatruni,¹ Arthur Barnard,³ Paul McEuen,^{3,4} and Michal Lipson**^{1,4}

¹*School of Electrical and Computer Engineering, Cornell University, Ithaca, New York 14853, USA.*

²*Instituto de Física, Universidade Estadual de Campinas, 13083-970, Campinas, SP, Brazil.*

³*Laboratory of Atomic and Solid State Physics, Cornell University, Ithaca, New York 14853, USA.*

⁴*Kavli Institute at Cornell for Nanoscale Science, Ithaca, New York 14853, USA.*

(Dated: June 6, 2012)

*These authors contributed equally to this work.

**To whom correspondence should be addressed; E-mail: ml292@cornell.edu

Synchronization, the emergence of spontaneous order in coupled systems, is of fundamental importance in both physical and biological systems. We demonstrate the synchronization of two dissimilar silicon nitride micromechanical oscillators, that are spaced apart by a few hundred nanometers and are coupled through optical radiation field. The tunability of the optical coupling between the oscillators enables one to externally control the dynamics and switch between coupled and individual oscillation states. These results pave a path towards reconfigurable massive synchronized oscillator networks.

Synchronization processes are part of our daily experiences as they occur widely in nature, for example in fireflies colonies¹, pacemaker cells in the heart², nervous systems³ and circadian cycles⁴. Synchronization is also of great technological interest since it provides the basis for timing and navigation⁵, signal processing⁶, microwave communication⁷, and could enable novel computing⁸ and memory concepts⁹. At the micro and nanoscale, synchronization mechanisms have the potential to be integrated with current nanofabrication capabilities and to enable scaling up to network sizes. The ability to control and manipulate such networks would enable to put in practice nonlinear dynamic theories that explain the behaviour of synchronized networks^{10,11}. Recent work on coupled spin torque^{7,12} and nanoscale electromechanical oscillators (NEMS)^{13,14} exhibit synchronized oscillation states. Major challenges with synchronized oscillators on the nanoscale are neighbourhood restriction and non-configurable coupling which limit the control, the footprint and possible topologies of complex oscillator networks^{15–17}. Here, we demonstrate the synchronization of two dissimilar silicon nitride (Si_3N_4) self-sustaining optomechanical oscillators coupled only through the optical radiation field as opposed to coupling through a structural contact or electrostatic interaction^{18,19}. The tunability of the optical coupling between the oscillators enables one to externally control the dynamics and switch between coupled and individual oscillation states. These results pave a path towards realizing synchronized micromechanical oscillators systems connected through optical links.

Optomechanical oscillators (OMOs) consist of cavity structures that support both tightly confined optical modes and long-living (high quality factor) mechanical modes^{20,21}. These modes can be strongly coupled: the cavity optical field leads to optical forces acting on the mechanical structure; mechanical displacements due to this force in turn affect the cavity optical field. Amplification or cooling of the mechanical modes of these cavities can be achieved by feeding these cavities with a continuous-wave (CW) laser²². The mechanical vibration

(driven by thermal Brownian motion) induces fluctuations of the cavity length, which translates into fluctuations of the optical resonant frequency; for a fixed-frequency driving laser this implies that the optical energy stored in the cavity also oscillates. Due to a finite cavity optical lifetime, the optical field does not respond instantaneously to the mechanical motion but instead oscillates with a slight phase lag; as the force that the optical field exerts on the mechanical mode is proportional to the stored optical energy, it will also experience such delay. Consequently the optical force will have one component that is in phase with the mechanical displacement, and another component that is 90° out of phase. When the laser is blue (red) detuned with respect to the optical mode frequency, the optical force component that is in phase with the mechanical vibration induces an optical spring effect that increases (reduces) the mechanical frequency²³, thus stiffening (softening) the mechanical spring. The out of phase component will decrease (increase) the effective mechanical damping, thus amplifying (cooling) the mechanical oscillation. Above a certain threshold laser power this optomechanical amplification overcomes the intrinsic mechanical damping; the device evolves from an optomechanical resonator to a self-sustaining optomechanical oscillator (OMO)¹⁶. The laser signal fraction that is transmitted, or reflected, from the optomechanical cavity becomes deeply modulated at the mechanical frequency of the oscillator^{20,24,25}.

Recently it has been predicted that a pair of OMOs could synchronize if they are optically coupled as opposed to mechanically coupled^{26,27}. Here we experimentally demonstrate the synchronization of two optically coupled OMOs [right (R) and left (L)] that are fabricated with slightly different dimensions (i.e. slightly different mechanical frequencies). The optical coupling means the mechanical displacement of one OMO will lead to a force on the other OMO through the optical field. This force is responsible for the effective mechanical coupling between the two OMOs. As the OMOs are pumped by a blue-detuned CW laser into self-sustaining os-

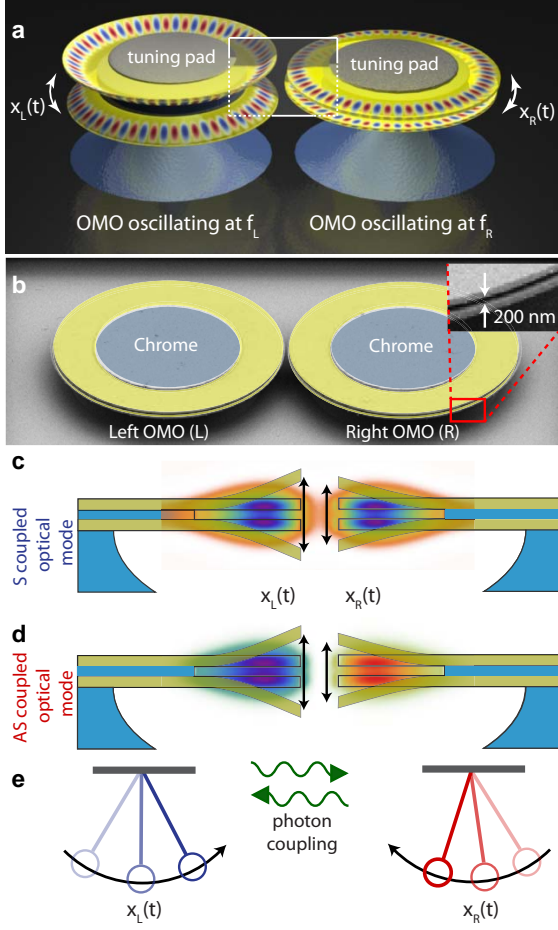


FIG. 1: Design of the optically coupled optomechanical oscillators (OMOs). (a) Schematic of the device illustrating the mechanical mode profile and the optical whispering gallery mode. (b) Scanning electron micrograph (SEM) image of the OMOs with chrome heating pads for optical tuning by top illumination. (c,d) The symmetric (S) and anti-symmetric (AS) coupled optical supermodes. The deformation illustrates the mechanical mode that is excited by the optical field. (e) The dynamics of the coupled OMOs can be approximated by a lumped model for two optically coupled damped-driven nonlinear harmonic oscillators.

oscillations, the R (L) OMO not only experiences the oscillation at its natural frequency but also a modulated optical force at the L (R) OMO's mechanical frequency. As the coupling between the two oscillators is increased, each OMO is eventually forced to oscillate at an intermediate frequency between their natural frequencies (Ω_R and Ω_L), that is, the onset of synchronization^{27–29}. We observe both the individual free-running and synchronized oscillation dynamics by switching on and off the purely optical coupling between two OMOs.

Each individual OMO, shown in figure 1a,b consists of two suspended vertically stacked Si_3N_4 disks. As illustrated in figure 1a, the optical and mechanical modes of such a cavity are localized around its free-standing edge. The disks are

fabricated using standard electron-beam lithography followed by dry and wet etching steps (see Methods). The two disks are 40 μm in diameter and 210 nm in thickness, while the air gap between them is 190 nm wide. Such a small gap and the relative low refractive index of Si_3N_4 ($n \approx 2.0$) induce a strong optical coupling between the top and bottom disks. The resonant frequency of the optical modes of the stacked disks depend strongly on their separation³⁰; therefore any mechanical vibration that modulates the vertical gap width also modulates the optical resonant frequency; a measure for the efficiency of this process is the optomechanical coupling, defined as $g_{\text{om}} = \partial\omega/\partial x$ where ω is the optical frequency and x is the mechanical mode amplitude^{20,30,31}. Our device exhibits a large optomechanical coupling, calculated to be $g_{\text{om}}/2\pi = 49$ GHz/nm (see SI). The mechanical mode that couples most strongly to the optical field is also illustrated by the deformation of the disks edge in figures 1a,c which has a natural frequency of $\Omega_m/2\pi \approx 50.5$ MHz. Note that variations in the fabrication process lead to different mechanical frequencies; indeed we show below that the two cavities are not identical and without the optical coupling they oscillate at different mechanical frequencies.

The two OMOs are separated by a distance of $d_g = (400 \pm 20)$ nm, minimizing direct mechanical coupling. This gap results in evanescent optical coupling between the OMOs when their optical resonant frequencies are close. The optical coupling leads to two optical supermodes spatially spanning both OMOs: a symmetric, lower frequency mode $b_+(t)$ (figure 1c) and an anti-symmetric higher frequency mode $b_-(t)$ (figure 1d). Their eigenfrequencies are given by $\omega_{\pm} = \bar{\omega} \pm \kappa/2$, where $\bar{\omega} = (\omega_L + \omega_R)/2$ and ω_L (ω_R) is the uncoupled optical resonant frequency of the L (R) OMO and κ is the optical coupling rate: a reflection of the distance between the two cavities. The mechanical modes of each cavity can be approximated by a lumped model consisting of two damped harmonic oscillators, which are driven by the optical supermode forces,

$$\ddot{x}_j + \Gamma_j \dot{x}_j + \Omega_j^2 x_j = F_{\text{opt}}^{(j)}(x_R, x_L)/m_{\text{eff}}^{(j)}, \text{ for } j, k = L, R \quad (1)$$

where x_j , Ω_j , Γ_j , $m_{\text{eff}}^{(j)}$ represent the mechanical displacement, mechanical resonant frequency, dissipation rate, and effective motional mass of each mechanical degree of freedom. The optical force is proportional to the optical energy stored in the coupled optical modes, which depend both on x_R and x_L , i.e. $F_{\text{opt}}^{(j)}(x_R, x_L) \propto |b_{\pm}(x_R, x_L)|^2$. Therefore the optical field not only drives but also mechanically couples each OMO. The nonlinear nature of this driving and coupling force form the basis for the onset of synchronization. In a first order linear approximation when the two OMOs are evenly coupled ($\omega_L = \omega_R$), the effective mechanical coupling force between the two oscillators is given by $F_{\text{coup}}^{(i)} = -k_I x_j + k_Q \dot{x}_j$ where k_I and k_Q are the position and velocity coupling coefficients (See supplementary information [SI] for details). These coupling coefficients are determined by both the input optical power P_{in} and laser-cavity detuning Δ as $k_I \propto \frac{P_{\text{in}} \Delta}{((\gamma/2)^2 + \Delta^2)^2}$

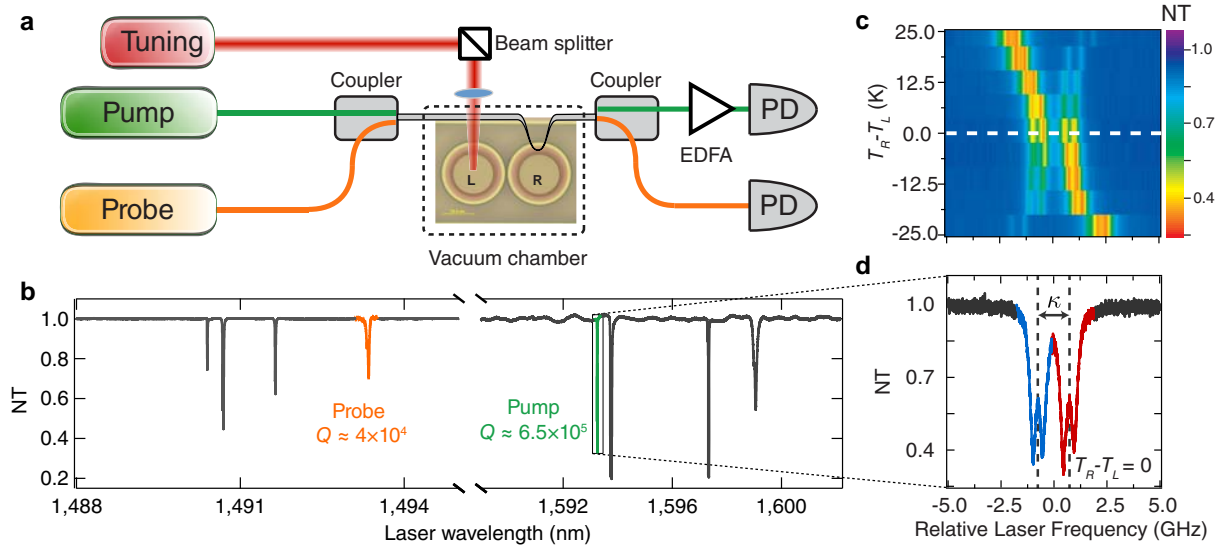


FIG. 2: Controlling the two OMO system. **(a)** Schematic of the experimental setup. The pump and probe light are launched together into the cavities and are detected separately by photodiodes (PD). An erbium doped fibre amplifier (EDFA) is used to amplify the transmitted signal to increase the signal strength. **(b)** Transmission spectrum of the coupled cavities. The green and orange coloured optical resonances correspond to the pump and probe resonances respectively. NT: normalized transmission. **(c)** Anti-crossing of the optical mode as the relative temperature of the L OMO (T_L) and the R OMO (T_R) is changed through varying the tuning laser power. The tuning laser is focused on to the two OMOs respectively to obtain the negative and positive relative temperatures. **(d)** Transmission spectrum of the maximally coupled state indicated by the white horizontal line in (c). The red (blue) part of the curve indicates the anti-symmetric (symmetric) optical supermode, κ is the optical coupling rate.

and $k_Q \propto \frac{P_{\text{in}}(\gamma/2)\Delta}{((\gamma/2)^2 + \Delta^2)^{3/2}}$ in the unresolved side band limit (optical damping rate $\gamma \ll \Omega_j$) as in our system. Therefore, by varying Δ and P_{in} , hence the effective mechanical coupling strength, synchronization of the two OMOs can be captured.

We experimentally demonstrate that the system can be re-configured to exhibit either coupled or single OMO dynamics by controlling the spatial distribution of the optical field between the two oscillators. While the distance between the two OMOs is fixed (i.e. fixed κ), their optical coupling can be turned off (on) through increasing (decreasing) the optical frequency mismatch $\delta = \omega_R - \omega_L$ between them. For large optical frequency mismatch among the two OMOs ($\delta \gg \kappa$) the supermodes reduce to the uncoupled optical modes of the individual OMO, $(b_+, b_-) \rightarrow (a_L, a_R)$. This can be readily seen from the expression of the optical supermodes amplitudes, which are given by linear combinations of the uncoupled modes of the left $a_L(t)$ and right $a_R(t)$ cavities: $b_{\pm}(t) = a_L(t) - a_R(t) i\kappa / (\delta \mp (\delta^2 - \kappa^2)^{1/2})$. We tune δ experimentally using thermo-optic effect, for which the optical frequency dependence on temperature can be approximated as $\omega_j(T_j) = \omega_0^{(j)} - g_{\text{th}}T_j$ for $j = L, R$, where $\omega_0^{(j)}$ is the intrinsic optical frequency and g_{th} is the thermal-optic tuning efficiency. The thermo-optic tuning is accomplished by focusing an out-of-plane laser beam with wavelength 1550 nm on either OMO (figure 2a). In order to increase the laser absorption, we deposit a 200 nm layer of chrome in the centre of

both OMOs (figure 2a,b). As heat is dissipated in the chrome pads, the cavity temperature increases and red shifts the optical resonance of the cavity through thermo-optic effect. A signature that the optical frequencies of both OMOs are matched is given by the almost symmetric resonance dips observed in the optical transmission spectrum (figure 2b, 2d), which also indicates maximum optical coupling between the cavity optical modes. We show experimentally that the coupling of the optical modes can be continuously tuned through changing the relative cavity temperature as in figure 2c. At $\Delta T = 0$ we have the maximum optical coupling, whereas for $\Delta T = \pm 25\text{K}$, the relative frequency difference is large ($\delta \gg \kappa$) and the optical mode in eq. (1) does not couple the two OMOs. They follow the usual single-cavity optomechanical dynamics²⁰.

We first characterize the individual dynamics of the two OMOs by switching their optical coupling off. This is achieved through increasing the heating laser power such that the temperature difference corresponds to the extremities in figure 2c. Each cavity is individually excited with a CW laser through a tapered optical fibre. As the laser frequency is tuned (from a higher to a lower frequency) into the optical resonance, the radio-frequency (RF) spectrum of the transmitted laser signal is detected by a photodiode (PD) and recorded using a RF spectrum analyser (RSA). The results revealing the single-cavity optomechanical dynamics are shown in figure 3a,b. The mechanical modes have natural mechanical frequencies of $(f_L, f_R) = (\Omega_L, \Omega_R)/2\pi = (50.283, 50.219)$ MHz,

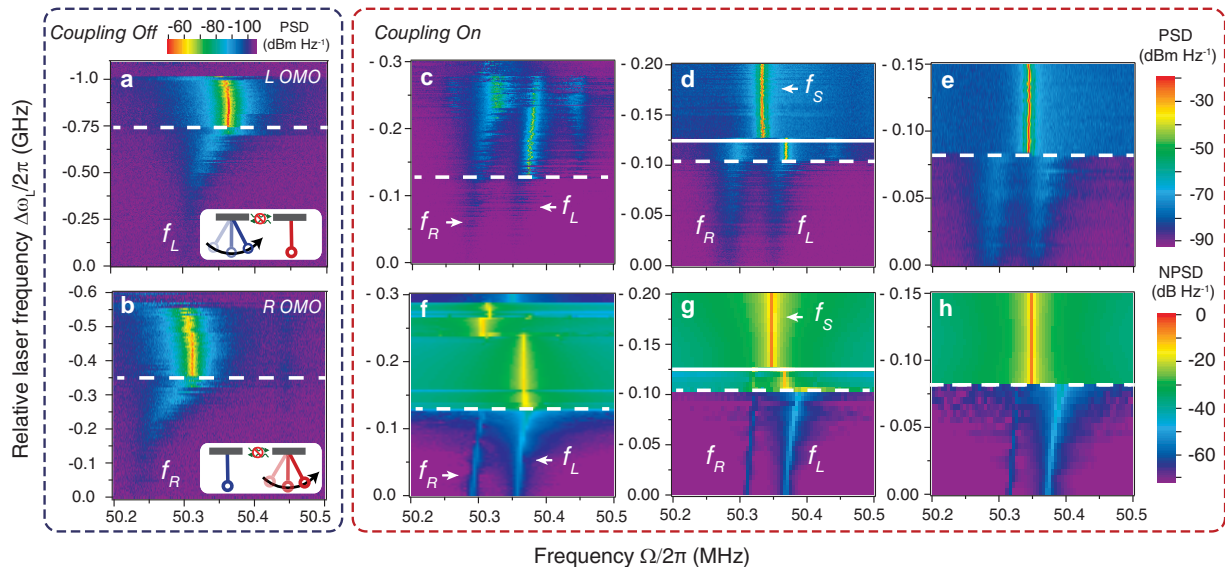


FIG. 3: RF spectra of the OMOs and synchronization (a, b) RF power spectra of cavity L (a) and R (b) as a function of laser frequency when the coupling is turned off. The horizontal white lines indicate the onset of self-sustaining oscillation. PSD: power spectral density. (c) When the coupling is turned on, at an input power $P_{in} = (1.8 \pm 0.2) \mu\text{W}$ cavities L and R do not synchronize and oscillate close to their natural frequencies (see SI). (d) At $P_{in} = (11 \pm 1) \mu\text{W}$ synchronization occurs after the horizontal solid white line. The synchronized frequency appears between the two cavities natural frequencies but only appear after a region of unsynchronized oscillation (between the dashed and solid white lines). (e) The system oscillate directly in a synchronized state at input optical power $P_{in} = (14 \pm 1) \mu\text{W}$. (f,g,h) Corresponding numerical simulations for the OMO system based on the lumped harmonic oscillator model illustrated in fig. 1d. NPSD: normalized power spectral density.

and intrinsic quality factors of $(Q_m^{(L)}, Q_m^{(R)}) = (3.4 \pm 0.3, 2.3 \pm 0.2) \times 10^3$. Due to the increased optomechanical back-action and intracavity optical power the OMOs have their frequencies increased (optical spring effect) and amplitudes grown as the laser is tuned into the optical resonance. Above a specific laser-cavity detuning, indicated by the horizontal white dashed lines on figure 3a,b the intrinsic mechanical losses are completely suppressed by the optomechanical amplification. At this point the optomechanical resonator starts self-sustaining oscillations and becomes an OMO characterized by sudden linewidth narrowing and oscillation amplitude growth^{15,16,27}. As the laser frequency sweeps away from the optical resonance it eventually reaches the point of maximum optical power coupled to the cavity; further sweeping can only reduce the optical power inside the cavity and the oscillation vanishes. It is clear from figure 3a,b that each cavity has only one mechanical mode in the frequency range of interest. Due to the slight difference in geometry, these frequencies differ by $\Delta f = f_L - f_R = (70.0 \pm 0.5) \text{ kHz}$.

We show the onset of spontaneous synchronization by sweeping the CW pump laser across the optical resonance, similarly to the single-cavity measurements above only now the optical coupling is switched on for coupled dynamics. Using the heating laser, we tune the optical coupling to its maximum value, indicated by the dashed-white line ($T_R - T_L = 0$) in figure 2c. The laser frequency sweeping is performed at

various optical power levels corresponding to different effective mechanical coupling strength. The optical power ranges from slightly above the estimated oscillation threshold (i.e weaker mechanical coupling for the L and R OMOs, $P_{th}^{(L,R)} \approx (640, 880) \text{ nW}$, up to several times their threshold power (i.e. stronger mechanical coupling). At a relative low input power, $P_{in} = (1.8 \pm 0.2) \mu\text{W}$, the mechanical peaks at f_R and f_L are simultaneously observed on the RF spectrum shown in figure 3c, below the dashed-white line. When the laser frequency is closer to the optical resonant frequency, more energy is available and the L OMO starts self-sustaining oscillation. Since cavity R has a higher oscillation threshold, due to its lower mechanical quality factor, it requires more optical power and only oscillates at a redder detuning; it can be noticed from figure 3c that both OMOs oscillate close to their natural frequency. Therefore they exhibit asynchronous oscillations at this lowest power level. At a higher input optical power level of $P_{in} = (11 \pm 1) \mu\text{W}$, the first oscillation takes place at $\Delta\omega_L/2\pi \approx -0.10 \text{ GHz}$, and similarly to the case shown in figure 3c, the L OMO oscillates first. However, as the laser frequency further moves into the optical resonance, there is enough energy for both OMOs to start self-sustaining oscillations; the two OMOs spontaneously oscillate in unison at an intermediate frequency of $f_S = \Omega_S/2\pi = 50.37 \text{ MHz}$ due to the increased effective mechanical coupling, which is a clear sign of synchronization. At this time, the output op-

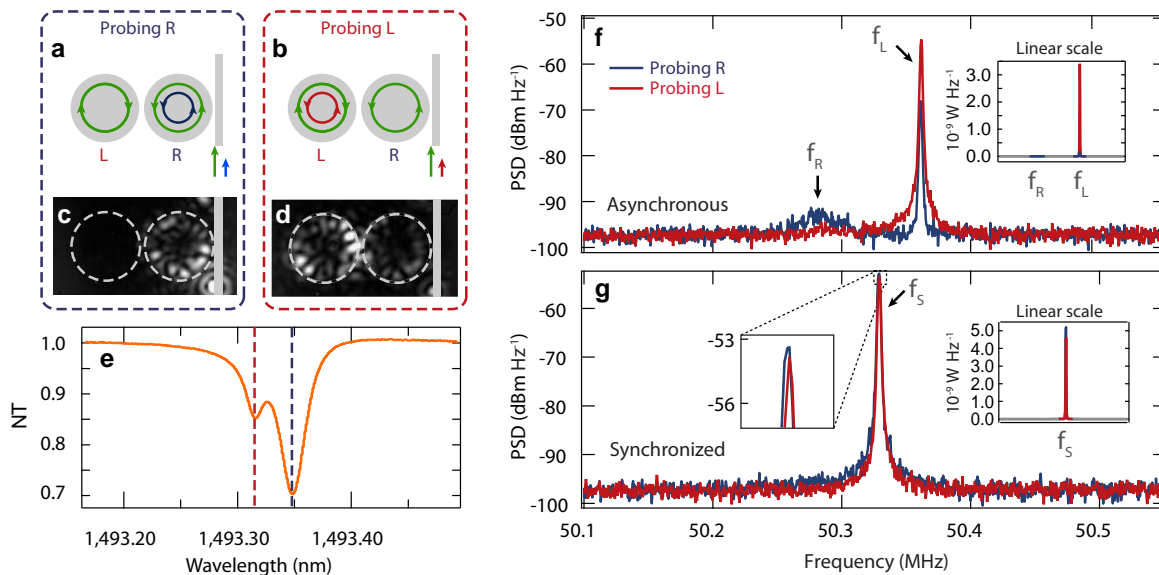


FIG. 4: Pump-probe measurement of the individual OMOs oscillation when coupled. The input pump power is $P_{in} = (11 \pm 1) \mu\text{W}$ as in fig. 3d. (a,b) Schematic of the pump-probe measurement principle. While the pump laser (green) is symmetrically shared between the two OMOs, the probe laser (blue for probing R and red for L) can measure each cavity selectively. (c,d) The uneven probe intensity distribution of the cavities, observed by an infrared CCD camera when the pump laser is off. (e) Normalized transmission (NT) spectrum for the probe resonances, which correspond to the orange resonances shown in fig. 2b. The red (blue) dashed line corresponds to the probe wavelength region for probing the L (R) OMO, as illustrated in (a,b). (f) The red (blue) curve is the L (R) cavity probe transmission RF spectrum, when the pump is in the asynchronous region $-0.13 < \Delta\omega_L/2\pi < -0.10$ GHz shown in fig. 3d; a strong peak at f_R is observed but with very different amplitude for two probing conditions. The right inset figures show the same curves in linear scale, emphasising the large difference between the blue and red curves. (g) Same curves shown in (f) but with the pump laser in the synchronous region $\Delta\omega_L/2\pi < -0.13$ GHz of fig. 3d. Here both cavities have similar amplitude at f_S , which can be clearly noticed in the linear scale inset.

tical RF power is increase by more than 5 dB in comparison with the L OMO oscillating only case showing that the two OMOs are phase-locked. At an even higher optical input power, $P_{in} = (14 \pm 1) \mu\text{W}$, the OMOs do not oscillate individually, instead they go directly into synchronized oscillations above the white-dashed line in figure 3e. We confirm that the OMOs are indeed synchronized by performing numerical simulations corresponding to each of the power levels we tested. The simulated spectra in figure 3f,g,h exhibit all the essential features observed and show good agreement with the measured spectra. It also allows us to confirm under which conditions the two OMOs are indeed oscillating (see Methods and SI).

To experimentally verify that both structures are indeed oscillating at the synchronized frequency, we probe the mechanical oscillation of each cavity individually. This demonstrates that the single oscillation peaks observed in figures 3d,e are not caused by one OMO resonantly driving the other; it also verifies that amplitude death of one of the OMOs does not occur, a known phenomenon in coupled nonlinear oscillators³². The transmitted pump laser signal only provides only global information of the coupled OMO system, it does not distinguishes the individual contribution from each OMO to the syn-

chronized signal. To overcome this we used a weak CW probe laser, as shown in the setup in figure 2a to excite an optical resonant mode that is not strongly coupled between the two OMOs; this scheme illustrated in figure 4a,b allows us to selectively probe the oscillations of the L or R OMO. Figure 4c,d show the uneven light intensity distribution that can be directly observed by capturing the scattered light with an infrared camera. The asymmetric splitting is also evident on the probe transmission shown in figure 4e. While these probe optical modes exhibit a low optical quality factor ($Q_{opt} \approx 4 \times 10^4$) that minimizes probe-induced perturbations to the mechanical oscillations, the pump laser power and sweep is identical to the one used figure 3d. When the L OMO is probed, and the pump detuning range is between the dashed and solid lines in figure 3d, the probe RF spectrum shows a strong peak at f_L , which is shown in the red curve in figure 4f. When the R OMO is probed, a peak also appears at this frequency, but it is 13 dB weaker as shown in the blue curve in figure 4f; a weak peak at f_R can also be noticed on the blue curve, indicating small amplitude oscillations of the R OMO. These results confirm that the oscillation state is very asynchronous in this detuning range with the L OMO oscillating at much larger amplitude. When the pump laser detuning is above the hor-

horizontal solid line in figure 3d there is only a single RF peak at the synchronized frequency f_S when probing either OMO (figure 4g); moreover, they differ in amplitude by less than 0.5 dB. This shows that both cavities are indeed oscillating with similar strength at the synchronized frequency.

We have demonstrated the onset of synchronization between two optomechanical oscillators coupled only through the optical radiation field. The ability to control the coupling strength are promising for realizing oscillator networks in which the oscillators can be addressed individually. Furthermore, established and future micro-photonics techniques such as electro-optic and thermo-optic techniques can now be extended to switch, filter and phase shift the coupling of these oscillators. Here we demonstrated coupling the near field between oscillators which can be switched on and off by thermo-optical means. In order to achieve long range coupling of mechanical oscillators, optical waveguides and optical fibres could be used enabling oscillator networks spread over large areas only limited by optical waveguide/fibre losses. Optically mediated mechanical coupling will also remove the restrictions of neighbourhood while creating 1D/2D/3D mechanical oscillator arrays³³. Using long range, directional and controllable mechanical coupling, synchronized optomechanical systems may enable a new class of devices in sensing, signal processing and on-chip non-linear dynamical systems¹⁷.

Methods

Coupled optical cavities A detailed model of this coupled optomechanical system is discussed in the SI; here we describe a simplified version that capture our system's essential aspects. The optical mode amplitudes are approximated by two coupled harmonic oscillator equations given by³⁴,

$$\begin{aligned} \dot{a}_j &= i\Delta_j a_j - (\gamma/2)a_j + i\kappa a_k + \sqrt{\gamma_e} s_j, \\ &\text{for } j, k = L, R, j \neq k \end{aligned} \quad (2)$$

where $\Delta_j = \omega - \omega_j(x_j, T_j)$ is the laser-cavity frequency detuning, ω is the optical frequency of the CW driving laser, $\omega_j(x_j, T_j)$ is the optical frequency of the each uncoupled optical mode ($a_{R,L}$), which depends both on each cavity temperature ($T_{R,L}$) and mechanical mode amplitude ($x_{R,L}$). The optical dissipation rate is given by γ and is assumed to be the same for both cavities; the coupling rate κ measures the evanescent field interaction of the two modes and couples the two optical cavities. The CW laser drive $\sqrt{\gamma_e} s_j$, which depends on the cavity coupling to the tapered fibre γ_e , only drives the a_R mode ($\sqrt{\gamma_e} s_L = 0$), resembling the experimental configuration shown in figure 2a where the tapered fibre excites only the rightmost cavity. Eqs. (2) can be diagonalized to yield the coupled optical modes (supermodes) we described in the main text.

Device Fabrication The two 210 nm thick stoichiometric Si_3N_4 films are deposited using low-pressure chemical vapour

deposition (LPCVD). The 190 nm SiO_2 layer is deposited by plasma-enhanced chemical vapour deposition (PECVD). The underlying substrate is a 4 μm SiO_2 formed by thermal oxidation of a silicon wafer. The OMOs are defined by electron beam lithography which is then patterned by reactive ion etching. The heater pads are subsequently defined by photolithography lift-off process. After defining the circular pads with lift-off resist, 200 nm of chrome is deposited on the device using electron beam evaporation and the residual chrome is lift-off afterwards. In order to release the structure, the device is immersed in buffered hydrofluoric acid (6 : 1) for an isotropic etch of the SiO_2 in between the disks and the substrate layer. The device is then dried with a critical point dryer to avoid stiction between the two Si_3N_4 disks.

Experimental setup The schematic for testing the OMO system is illustrated in figure 2a. Two tunable external cavity diode lasers are combined using a 3dB directional coupler to an optical fiber that is fed into a vacuum probe station. Inside the vacuum chamber, the tapered fiber is positioned close to the OMO of interest to allow evanescent coupling using a micropositioning system. The output light is then splitted by a WDM splitter to a New Focus 1811 (125 MHz bandwidth) photodetector. Since the power level we use to test for our device is low, an erbium doped fibre preamplifier is used to amplify the output signal and improve signal-to-noise ratio in the detector. The electronic signal from the detector is split and fed to an oscilloscope to observe the time waveform and to RSA for the frequency spectrum. To obtain the RF map, the laser is configured to sweep from the blue side of the resonance to the red side in a stepwise fashion by applying an external voltage to the laser cavity piezo-transducer. At each frequency step, a snap-shot of the RF spectrum is recorded with 1 kHz resolution bandwidth and 100 Hz video bandwidth.

Simulation The optical and mechanical quality factors are obtained by non-linear least square fitting to the measured optical and RF spectrum. The measured mechanical and optical frequencies, and their respective quality factors are fed as parameters to the lumped model described by eqs. (1) and (2). Other parameters such as the effective motional mass m_{eff} and the optomechanical coupling g_{om} are obtained from finite element simulations (FEM). From these measured and calculated parameters we estimate the threshold power from the expression $P_{\text{th}} = m_{\text{eff}} \Omega_m \omega_0^4 (4Q_m Q^3 (g_{\text{om}})^2 \eta_c)^{-1}$, where $\eta_c = \gamma_e / (\gamma)$ is the coupling ideality factor. Due to nonlinear dependence on most parameters, such as Q and g_{om} the error propagation is large in the estimated threshold power. The error propagation in the threshold estimation is detailed in the SI, where we estimate an overall error of $\delta P_{\text{th}} / P_{\text{th}} = 35\%$. To obtain the density plots shown in figure 3 we feed the dynamical model described in the main text, and detailed in the SI, with the measured and calculated parameters. The simulations are performed at various power levels close to the experimentally measured power. The optimum power matching was chosen to match the laser frequencies at which the bifurcations take place in the experimental data.

Acknowledgement

This work was supported in part by the National Science Foundation under grant 0928552. The authors gratefully acknowledge the partial support from Cornell Center for Nanoscale Systems which is funded by the National Science Foundation and funding from IGERT: A Graduate Traineeship in Nanoscale Control of Surfaces and Interfaces (DEG-0654193). This work was performed in part at the Cornell Nano-Scale Science & Technology Facility (a member of the National Nanofabrication Users Network) which is supported by National Science Foundation, its users, Cornell University and Industrial users. G.S.W acknowledges FAPESP and CNPq INCT Fotonicom for financial support in Brazil. We acknowledge Paulo Nussenzveig, Richard Rand and Steven

Strogatz for fruitful discussion about our results.

Author Contributions

M. Z. and G.W designed, fabricated and tested the devices. S. M. designed and simulated the devices. A. B. designed the experimental setup and helped testing. P.M. and M.L supervised all stages of the experiment. All authors discussed the results and their implications and contributed to writing this manuscript.

Competing Interest

The authors declare that they have no competing financial interests. Correspondence and requests for materials should be addressed to M.L. (email: ml292@cornell.edu)

-
- ¹ Buck, J. & Buck, E. Mechanism of rhythmic synchronous flashing of fireflies. fireflies of southeast asia may use anticipatory time-measuring in synchronizing their flashing. *Science* **159**, 1319–27 (1968). [1](#)
- ² Peskin, C. S. *Mathematical aspects of heart physiology* (Courant Institute of Mathematical Sciences, New York University, New York, 1975). [1](#)
- ³ Whittington, M. A., Traub, R. D. & Jefferys, J. G. Synchronized oscillations in interneuron networks driven by metabotropic glutamate receptor activation. *Nature* **373**, 612–5 (1995). [1](#)
- ⁴ Strogatz, S. H. *Sync: the emerging science of spontaneous order* (Hyperion, New York, 2003), 1st edn. [1](#)
- ⁵ Bahder, T. B. *Clock synchronization and navigation in the vicinity of the earth* (Nova Science, New York, 2009). [1](#)
- ⁶ Bregni, S. *Synchronization of digital telecommunications networks* (Wiley, Chichester, 2002). [1](#)
- ⁷ Kaka, S. *et al.* Mutual phase-locking of microwave spin torque nano-oscillators. *Nature* **437**, 389–92 (2005). [1](#)
- ⁸ Mahboob, I. & Yamaguchi, H. Bit storage and bit flip operations in an electromechanical oscillator. *Nature Nanotechnology* **3**, 275–279 (2008). [1](#)
- ⁹ Bagheri, M., Poot, M., Li, M., Pernice, W. P. H. & Tang, H. X. Dynamic manipulation of nanomechanical resonators in the high-amplitude regime and non-volatile mechanical memory operation. *Nature Nanotechnology* (2011). [1](#)
- ¹⁰ Watts, D. J. & Strogatz, S. H. Collective dynamics of small-world networks. *Nature* **393**, 440–442 (1998). [10.1038/30918](#). [1](#)
- ¹¹ Hoppensteadt, F. & Izhikevich, E. Synchronization of mems resonators and mechanical neurocomputing. *Ieee Transactions On Circuits and Systems I-Fundamental Theory and Applications* **48**, 133–138 (2001). [1](#)
- ¹² Mancoff, F., Rizzo, N., Engel, B. & Tehrani, S. Phase-locking in double-point-contact spin-transfer devices. *Nature* **437**, 393–395 (2005). [1](#)
- ¹³ Shim, S.-B., Imboden, M. & Mohanty, P. Synchronized oscillation in coupled nanomechanical oscillators. *Science* **316**, 95–99 (2007). [1](#)
- ¹⁴ Zalalutdinov, M. *et al.* Frequency entrainment for micromechanical oscillator. *Applied Physics Letters* **83**, 3281–3283 (2003). [1](#)
- ¹⁵ Heinrich, G., Ludwig, M., Qian, J., Kubala, B. & Marquardt, F. Collective dynamics in optomechanical arrays. *Physical Review Letters* **107**, 043603 (2011). [1](#), [4](#), [17](#)
- ¹⁶ Marquardt, F., Harris, J. & Girvin, S. Dynamical multistability induced by radiation pressure in high-finesse micromechanical optical cavities. *Physical Review Letters* **96**, 103901 (2006). [1](#), [4](#), [15](#), [16](#), [17](#)
- ¹⁷ Marquardt, F. Quantum mechanics: The gentle cooling touch of light. *Nature* **478**, 47–8 (2011). [1](#), [6](#)
- ¹⁸ Buks, E. & Roukes, M. Electrically tunable collective response in a coupled micromechanical array. *Journal of Microelectromechanical Systems* **11**, 802–807 (2002). [1](#)
- ¹⁹ Karabalin, R. B., Cross, M. C. & Roukes, M. L. Nonlinear dynamics and chaos in two coupled nanomechanical resonators. *Physical Review B* **79**, 165309 (2009). [1](#)
- ²⁰ Kippenberg, T. & Vahala, K. Cavity opto-mechanics. *Optics Express* **15**, 17172–17205 (2007). [1](#), [2](#), [3](#), [10](#), [15](#), [16](#)
- ²¹ Braginsky, V., Strigin, S. & Vyatchanin, S. Parametric oscillatory instability in fabry-perot interferometer. *Physics Letters a* **287**, 331–338 (2001). [1](#)
- ²² Arcizet, O., Cohadon, P., Briant, T., Pinard, M. & Heidmann. Radiation-pressure cooling and optomechanical instability of a micromirror. *Nature* **444**, 71–74 (2006). [1](#)
- ²³ Sheard, B., Gray, M., Mow-Lowry, C., McClelland, D. & Whitcomb, S. Observation and characterization of an optical spring. *Physical Review a* **69**, 051801 (2004). [1](#)
- ²⁴ Carmon, T., Rokhsari, H., Yang, L., Kippenberg, T. J. & Vahala, K. J. Temporal behavior of radiation-pressure-induced vibrations of an optical microcavity phonon mode. *Physical Review Letters* **94**, 223902 (2005). [1](#), [15](#)
- ²⁵ Grudinin, I. S., Lee, H., Painter, O. & Vahala, K. J. Phonon laser action in a tunable two-level system. *Physical Review Letters* **104**, 083901 (2010). [1](#), [15](#)
- ²⁶ Manipatruni, S., Wiederhecker, G. & Lipson, M. Long-range synchronization of optomechanical structures. In *Quantum Electronics and Laser Science Conference, QWII* (Optical Society of America, 2011). [1](#)
- ²⁷ Holmes, C. A., Meaney, C. P. & Milburn, G. J. Multi-stability and synchronization of many nano-mechanical resonators coupled via a cavity field. *arXiv e-prints: 1105.2086* (2011). [1](#), [2](#), [4](#), [16](#), [17](#), [20](#)
- ²⁸ Cross, M., Zumdieck, A., Lifshitz, R. & Rogers, J. Synchronization by nonlinear frequency pulling. *Physical Review Letters* **93**,

- 224101 (2004).
- ²⁹ Hossein-Zadeh, M. & Vahala, K. Observation of injection locking in an optomechanical rf oscillator. *Applied Physics Letters* **93**, 191115–191115–3 (2008). [2](#)
- ³⁰ Wiederhecker, G. S., Chen, L., Gondarenko, A. & Lipson, M. Controlling photonic structures using optical forces. *Nature* **462**, 633–U103 (2009). [2](#)
- ³¹ Wiederhecker, G. S., Manipatruni, S., Lee, S. & Lipson, M. Broadband tuning of optomechanical cavities. *Optics Express* **19**, 2782–2790 (2011). [2](#)
- ³² Mirollo, R. & Strogatz, S. Amplitude death in an array of limit-cycle oscillators. *Journal of Statistical Physics* **60**, 245–262 (1990). [5](#)
- ³³ Arlett, J. L., Myers, E. B. & Roukes, M. L. Comparative advantages of mechanical biosensors. *Nature Nanotechnology* **6**, 203–15 (2011). [6](#)
- ³⁴ Haus, H. A. *Waves and fields in optoelectronics* (Prentice-Hall, Englewood Cliffs, NJ, 1984). [6](#), [13](#)
- ³⁵ Anetsberger, G. *et al.* Near-field cavity optomechanics with nanomechanical oscillators. *Nature Physics* **5**, 909–914 (2009). [10](#)
- ³⁶ Eichenfield, M., Chan, J., Safavi-Naeini, A. H., Vahala, K. J. & Painter, O. Modeling dispersive coupling and losses of localized optical and mechanical modes in optomechanical crystals. *Optics Express* **17**, 20078–20098 (2009). [11](#)
- ³⁷ Johnson, S. *et al.* Perturbation theory for maxwell’s equations with shifting material boundaries. *Physical Review E* **65**, 066611 (2002). [11](#)
- ³⁸ Gorodetsky, M., Pryamikov, A. & Ilchenko, V. Rayleigh scattering in high-q microspheres. *Journal of the Optical Society of America B-Optical Physics* **17**, 1051–1057 (2000). [13](#)
- ³⁹ Spillane, S., Kippenberg, T., Painter, O. & Vahala, K. Ideality in a fiber-taper-coupled microresonator system for application to cavity quantum electrodynamics. *Physical Review Letters* **91**, 043902 (2003). [13](#), [18](#)
- ⁴⁰ Law, C. K. Interaction between a moving mirror and radiation pressure: A hamiltonian formulation. *Phys. Rev. A* **51**, 2537–2541 (1995). [15](#)
- ⁴¹ Eichenfield, M., Camacho, R., Chan, J., Vahala, K. J. & Painter, O. A picogram- and nanometre-scale photonic-crystal optomechanical cavity. *Nature* **459**, 550–555 (2009). URL <http://dx.doi.org/10.1038/nature08061>. [15](#), [16](#)
- ⁴² Saulson, P. Thermal noise in mechanical experiments. *Physical Review D* **42**, 2437–2445 (1990). [19](#)
- ⁴³ Hauschildt, B., Janson, N. B., Balanov, A. & Schoell, E. Noise-induced cooperative dynamics and its control in coupled neuron models. *Physical Review E* **74**, 051906 (2006). [19](#)
- ⁴⁴ Hoeye, S., Suarez, A. & Sancho, S. Analysis of noise effects on the nonlinear dynamics of synchronized oscillators. *Ieee Microwave and Wireless Components Letters* **11**, 376–378 (2001). [19](#)
- ⁴⁵ Burrage, K., Burrage, P., Higham, D. J., Kloeden, P. E. & Platen, E. Comment on ”numerical methods for stochastic differential equations”. *Physical Review E* **74**, 068701 (2006). [19](#)
- ⁴⁶ Kloeden, P. E. & Platen, E. *Numerical solution of stochastic differential equations*, vol. 23 (Springer, Berlin, 1999), corr. 3rd print edn. URL <http://www.loc.gov/catdir/enhancements/fy0812/00266312-d.html>.
- ⁴⁷ Wilkie, J. Numerical methods for stochastic differential equations. *Physical Review E* **70**, 017701 (2004). [19](#)

Supplementary Information

Contents

S1. Experimental Methods	9
A. Detailed experimental setup	9
B. Measurements	10
C. Single and coupled cavities measurement	10
D. Pump probe measurement	10
E. RF time-domain output power	11
S2. Lumped Model Parameters	11
A. Optical and Mechanical modes	11
B. Top illumination thermal tuning	11
S3. Coupled Optomechanical Oscillators	13
A. Coupled mode equations	13
B. Steady-state transmission	13
C. Intrinsic mechanical frequencies	14
D. Mechanical equations and optomechanical coupling	15
E. Optical transduction of mechanical oscillations	15
S4. Toy model for synchronization	16
A. Optically mediated mechanical coupling	16
B. Approximate Kuramoto model	18
C. Oscillation treshold	18
S5. Synchronization Simulation	19
A. Simulation approach	19
B. Simulation results	20

S1. EXPERIMENTAL METHODS

A. Detailed experimental setup

We measure the optomechanical transduction of the coupled OMOs using the setup shown in figure [S1](#). The green (red) line indicates the pump (probe) laser path. The probe is only used when taking the pump-probe measurements. The radio frequency (RF) spectral maps shown in the main text and in figure [S1](#) are obtained with the probe laser off. Both the pump and the probe laser are fibre-coupled, tunable, near-infra (IR) lasers (Tunics Reference and Ando AQ4321D). Their optical power is controlled using independent variable optical attenuators. The pump and probe light are individually sent to a polarization controller and combined with a 50 : 50 directional fiber coupler. A fraction of the power is monitored by a power meter which indicates the equivalent input optical power to the system. To prevent the back scattered light from entering the laser, an optical isolator is used before feeding the laser into a vacuum probe station (Lakeshore TTPX) operating at a pressure of 10^{-5} mT. The light is evanescent coupled to the OMOs through a tapered optical fibre waveguide by using a micro positioning system.

A small portion of the transmitted light (10%) is also monitored by a power meter. The remaining transmitted light is split with a wavelength division multiplexing coupler to separate the pump and the probe laser. Since the pump power used is low, especially for sub-threshold measurements, the pump light is optionally amplified with a low noise erbium pre-amplifier (EDFA, Amonics AEDFA-PL-30) before coupling to a 125 MHz bandwidth photodiode (New Focus 1181). An additional detector (Thorlabs PDB150C-AC) can be switched on when the probe measurement is necessary. Half of the detected signal is sent to an oscilloscope and the remaining is coupled to a radio-frequency spectrum analyser (RSA, Agilent E4407B).

The heating light source is provided by another near-IR laser (JDS SWS16101), operating at 1550 nm, and amplified by a high power EDFA (Keopsys KPS-CUS-BT-C-35-PB-111-FA-FA) that can provide a maximum power of 2 W. The light is sent to the microscope optics which focus the light on to the device. Typically, 50 mW of laser power is needed to achieve the desired tuning range, details of tuning aspect can be found in section [S2B](#).

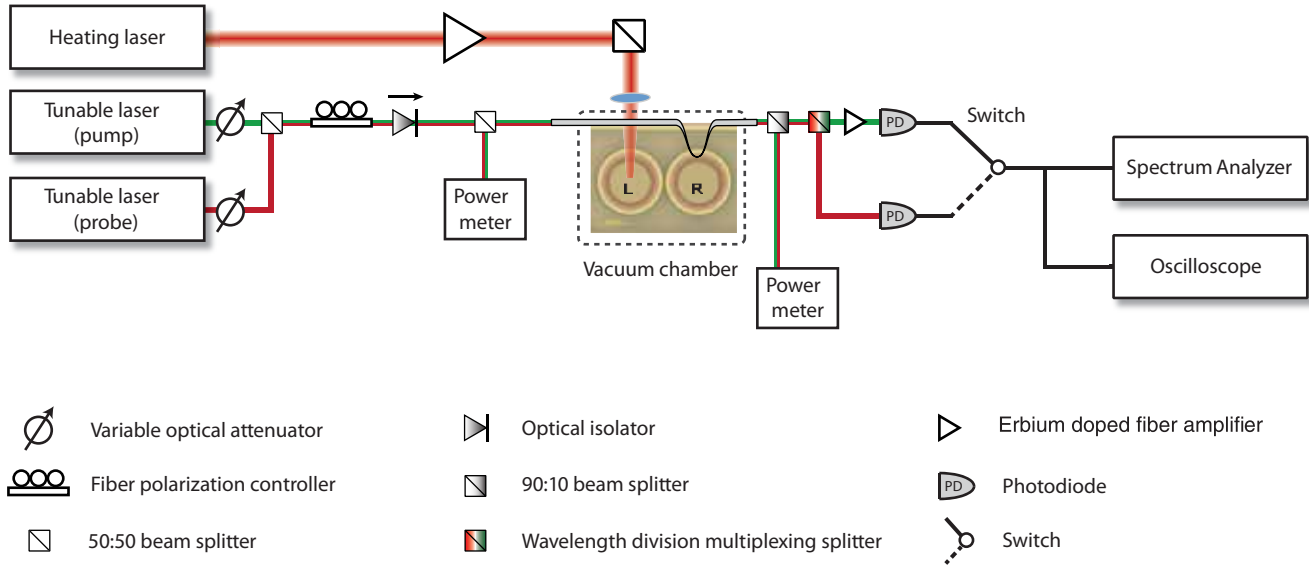


FIG. S1: Detailed experimental setup. See SI text for more details.

B. Measurements

The RF spectral maps are obtained by detuning the laser from blue to red into the optical resonance in a stepwise fashion, as controlled by a voltage applied to laser's external cavity piezo; the laser used has a tuning coefficient of 1.1 GHz/volt. For each voltage step, the RF spectrum is recorded. Therefore, the step size determines the vertical resolution of the RF spectra map (see Fig.3 main text) whereas the resolution bandwidth of the RSA determines the horizontal resolution. Here we used a detuning step size of 3 MHz and a resolution bandwidth of 1 kHz (100 Hz video bandwidth). This allows us to obtain a high resolution map while keeping the data collection time reasonable (≈ 20 minutes).

C. Single and coupled cavities measurement

The single cavity data are obtained by coupling the tapered fiber either to the L or R OMO. When one OMO is tested, the remaining one is heated by the heating laser with high power (~ 50 mW) to ensure that they are completely decoupled. The coupled cavity data are obtained by coupling to the R OMO with the tapered fibre. In this case we use the external heating laser to fine tune the coupling so that their split spectrum is symmetric.

D. Pump probe measurement

The pump probe measurements provide direct evidence for the synchronization of the two OMOs. The individual probe of each cavity, as shown in Fig. 4 main text, relies on the asymmetric coupling of one the higher order optical supermodes. This asymmetry arises due to their different optical resonant frequency (See section S2 A) which stems from the slight difference in the geometry of the two OMOs. This leads to a different mode splitting for the higher and lower order optical modes. In the devices we have tested, the majority of them show similar non-identical mode splitting.

Due to its lowers optical quality factor (Q) and reduced optomechanical coupling g_{om} , the threshold power for self-sustaining oscillations^{20,35} of the probe resonance is $P_{th_{probe}} \approx 20$ mW, which is roughly 20,000 times larger than the pump resonance threshold optical power $P_{th_{pump}} \approx 1$ μ W. We used a probe power of $P_p = (20 \pm 2)$ μ W, ensuring a low-noise detected probe signal without affecting the cavity oscillation dynamics.

E. RF time-domain output power

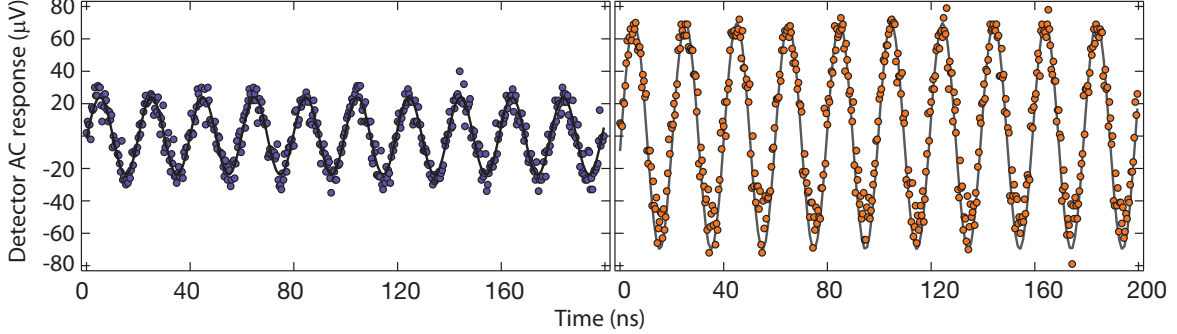


FIG. S2: Detector voltage time trace for the L OMO oscillating only state (left) and the synchronized state (right). The synchronized optical RF power is more than 3 time higher than the L OMO oscillating only state.

We record the real-time trace of the output detector signal with an oscilloscope for both the asynchronous state (between dashed and solid line in Fig 3c) and the synchronized state (above solid line in Fig 3c). As shown in the RF power spectrum in Fig 3d and figure S2 The oscillation output RF power is increased by more than 5 dB as a the two OMO synchronizes. This is expected as both OMOs contribute to the total output optical RF power.

S2. LUMPED MODEL PARAMETERS

A. Optical and Mechanical modes

To obtain the optical and mechanical modes of the optomechanical disk cavity we rely on finite element simulations using COMSOL®. From these numerical simulations we derive parameters for the lumped model that describes the optomechanical dynamics, such as the effective motional mass m_{eff} , and the optomechanical coupling rate g_{om} . The optical modes are sought by solving the Helmholtz vector wave equation with an ansatz $\mathbf{E}(r, z, \phi) = \mathbf{E}(r, z) \exp(im\phi)$. In the table S1 we show the mode radial electric field profile for the lowest order optical transverse-electric (TE) modes. The mechanical displacement field is sought by enforcing complete cylindrical symmetry, $\mathbf{u}(r, \phi, z) = \mathbf{u}(r, z)$, the mode profiles are also shown on table S1. From the sought eigenmodes, the optomechanical coupling coefficients for the supported optical modes are calculated using boundary perturbation theory^{36,37},

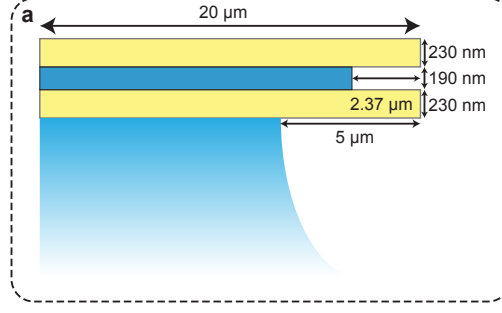
$$g_{om} \equiv \frac{\partial \omega}{\partial x} = \frac{\omega_0}{2} \frac{\int (\mathbf{U} \cdot \hat{n}) \left(\Delta \epsilon_{12} |\mathbf{E} \cdot \hat{t}|^2 + \Delta \epsilon_{12}^{-1} |\mathbf{D} \cdot \hat{n}|^2 \right) dA}{\int \epsilon |\mathbf{E}|^2 dV}, \quad (\text{S1})$$

where the dimensionless displacement field is defined as $\mathbf{U} \equiv \mathbf{u} / \max |\mathbf{u}|$, the relative permittivity differences are given by $\Delta \epsilon_{12} = \epsilon_1 - \epsilon_2$ and $\Delta \epsilon_{12}^{-1} = 1/\epsilon_1 - 1/\epsilon_2$, the unit vectors \hat{t} and \hat{n} indicate the tangential and normal components of the vectors. The effective motional mass is calculated as,

$$m_{eff} = \int \rho |\mathbf{U}|^2 dV. \quad (\text{S2})$$

B. Top illumination thermal tuning

The coupling between the cavities is controlled by changing their resonant frequencies through the thermo-optic effect. We choose to use 200 nm thick chrome pads as the heating element since they absorb 25% of 1550 nm light at normal incidence, taking into account its reflectivity. Chrome is also resistant to buffered oxide etch which follows in the fabrication steps. The 1550 nm laser is amplified with an EDFA, coupled to the imaging microscope and focused on the chrome pads. The heat



Mechanical mode	$\frac{\Omega_m}{2\pi}$ (MHz)	m_{eff} (pg)
	50.5	110
	28.7	194

Profile ($ \mathbf{E} \cdot \hat{r} $)	Mode TE_m^n	λ_0 (nm)	$g_{om}/2\pi$ (GHz/nm)
	TE_{115}^1	1582.28	49.4
	TE_{110}^2	1584.87	11.3
	TE_{106}^3	1582.31	17.9
	TE_{101}^4	1591.01	10.6

TABLE S1: Optical and mechanical modes parameters. (a) Geometry of the optomechanical cavity used to calculate the modes and parameters shown in the tables. For the optical modes profiles, it is shown the modulus of the radial electric field $|\mathbf{E} \cdot \hat{r}|$; g_{om} is calculated using Eq. (S1). whereas for the mechanical modes it is shown the displacement amplitude $|u|$ as colors and the deformation represents the normalized displacement.

absorbed by the chrome pads induces a temperature change $\Delta T = R_{th}P_{abs}$, where $R_{th} = \partial\Delta T/\partial P_{abs} \approx 5.2 \times 10^3$ K/W is the simulated effective thermal resistance of our device. Due to thermo-optic effect, the temperature frequency shift rate is given by the perturbation expression,

$$g_{th} = \frac{\partial\omega_T}{\partial\Delta T} = -\frac{\omega_0}{2n_g} \frac{\int \alpha(r, z)T_{rel}(r, z)|\mathbf{E}|^2 dV}{\int |\mathbf{E}|^2 dV} \quad (\text{S3})$$

where $0 < T_{rel}(r, z) < 1$ is the dimensionless relative temperature distribution of the device, α is the material-dependent thermo-optic coefficient, and n_g is the optical mode group index. If we define the overlap integral $\Gamma = \int_{SiN} |\mathbf{E}|^2 / \int_{all} |\mathbf{E}|^2$, Eq. (S3) is approximately given by $g_{th} \approx -(T_{rel}^{(SiN)})\omega_0\alpha_{SiN}\Gamma/(2n_g)$. In Fig. S3 we show the simulated relative temperature field $T_{rel}(r, z)$, at the edge of the disk $T_{rel} = T_{rel}^{(SiN)} \approx 0.83$. From these results we can estimate the top illumination laser power needed to tune the cavity's optical frequency by $\Delta\omega_T$,

$$P_{abs} = \frac{\Delta\omega_T}{g_{th}R_{th}} \approx \frac{2n_g}{R_{th}(T_{rel}^{(SiN)})\alpha_{SiN}\Gamma} \left(\frac{\Delta\omega_T}{\omega_0} \right) \quad (\text{S4})$$

For our device, tuning of $\delta\lambda \approx 0.2$ nm is sufficient to completely decouple the two cavity modes. Using $n_g \approx 1.8$, $\alpha_{SiN} = 3 \times 10^{-5}$ K $^{-1}$, and $\Gamma \approx 0.59$, Eq. (S4) gives a tuning efficiency $g_{th}/2\pi \approx -256$ MHz/K, therefore a laser power of $P =$

$P_{abs}/25\% \approx 24$ mW is needed to control the optical coupling between the cavities (see section S3 B). This value is in reasonable agreement with the experimental power range.

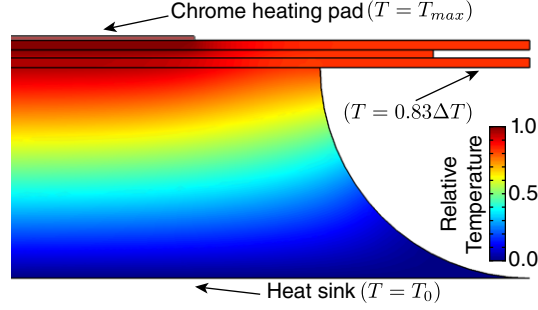


FIG. S3: Thermal tuning of optical resonances. Simulated temperature ($\Delta T = T - T_0$) profile of the optical micro cavity. The bottom boundary act as a heat reservoir with constant temperature $T_0 = 300$ K. In the mirroring edge, where the optical modes are localized, the temperature is $T \approx 0.83\Delta T$

S3. COUPLED OPTOMECHANICAL OSCILLATORS

A. Coupled mode equations

The optical modes a_1 and a_2 of each optical cavity are coupled through the optical near-field. Due to scattering, there is also coupling between the clockwise (cw) and counter-clockwise (ccw) optical modes, therefore we need to consider four optical modes, $a_1^{(cw,ccw)}$ and $a_2^{(cw,ccw)}$. The coupled equations satisfied by these modes are given by^{34,38},

$$\begin{pmatrix} \dot{a}_1^{cw} \\ \dot{a}_1^{ccw} \\ \dot{a}_2^{cw} \\ \dot{a}_2^{ccw} \end{pmatrix} = \begin{pmatrix} -\frac{\gamma_1}{2} - i\omega_1 & \frac{i\beta}{2} & \frac{i\kappa}{2} & 0 \\ \frac{i\beta}{2} & -\frac{\gamma_1}{2} - i\omega_1 & 0 & \frac{i\kappa}{2} \\ \frac{i\kappa}{2} & 0 & -\frac{\gamma_2}{2} - i\omega_2 & \frac{i\beta}{2} \\ 0 & \frac{i\kappa}{2} & \frac{i\beta}{2} & -\frac{\gamma_2}{2} - i\omega_2 \end{pmatrix} \begin{pmatrix} a_1^{cw} \\ a_1^{ccw} \\ a_2^{cw} \\ a_2^{ccw} \end{pmatrix} + \sqrt{\gamma_1\eta_c}s_1(t) \begin{pmatrix} 1 \\ 0 \\ 0 \\ 0 \end{pmatrix} \quad (\text{S5})$$

where ω_m are optical resonance angular frequencies, γ_m is total damping rate, $\kappa/2$ is the inter-cavity optical coupling rate, and $\eta_c = \gamma_e/(\gamma_{i1} + \gamma_e)$ is the coupling ideality factor, where γ_e is the external loss rate (due to the bus waveguide) and γ_i is the intrinsic damping rate³⁹.

The system of Eqs. (S5) can be diagonalized exactly, each eigenvector is governed by an equation of the form

$$\dot{b}_{(m,\pm)} = [-i(\bar{\omega} + (-1)^m \xi/2 \pm \beta/2) - \bar{\gamma}/2] b_{(m,\pm)}(\pm)^m \frac{\kappa\sqrt{\gamma_1\eta_c}s_1(t)}{2\xi}, \text{ for } m = 1, 2, \quad (\text{S6})$$

where $\bar{\omega} = (\omega_1 + \omega_2)/2$, $\bar{\gamma} = (\gamma_1 + \gamma_2)/2$ and $\xi = \kappa\sqrt{1 - (\delta/\kappa)^2}$, where $\delta = (\gamma_1 - \gamma_2)/2 + i(\omega_2 - \omega_1)$. The original fields $a_{1,2}^{cw,ccw}$ can be recovered from the eigenvectors through the relation,

$$\begin{pmatrix} a_1^{cw} \\ a_1^{ccw} \\ a_2^{cw} \\ a_2^{ccw} \end{pmatrix} = \frac{1}{2\xi} \begin{pmatrix} -\kappa b_{(1,-)} + (\xi + i\delta)b_{(2,-)} \\ -\kappa b_{(1,+)} + (\xi + i\delta)b_{(2,+)} \\ \kappa b_{(1,-)} + (\xi - i\delta)b_{(2,-)} \\ \kappa b_{(1,+)} + (\xi - i\delta)b_{(2,+)} \end{pmatrix} \quad (\text{S7})$$

where $b_{(m,\pm)} = (a_m^{ccw} \pm a_m^{cw})$, Eq. (S7) will be used to calculate the optical transmission function in the section S3 B below.

B. Steady-state transmission

To obtain the low-power steady-state optical transmission spectrum, we assume that the laser driving term in Eq. (S5) is oscillating at ω , i.e., $s_1(t) = s_1 e^{i\omega t}$. Eq. (S6) can be written in a rotating frame $c_{(m,\pm)}(t) = \tilde{c}_{(m,\pm)}(t) e^{i\omega t}$. The resulting

equations will be of the form,

$$\dot{\tilde{b}}_{(m,\pm)} = [i\Delta_{(m,\pm)} - \bar{\gamma}/2] \tilde{b}_{(m,\pm)}(\pm)^m \frac{\kappa s_1 \sqrt{\gamma_1 \eta_c}}{2\xi}, \text{ for } m = 1, 2, \quad (\text{S8})$$

where $\Delta_{(m,\pm)} = \omega - (\bar{\omega} + (-1)^m \xi/2 \pm \beta/2)$ is the laser-cavity frequency detuning for each of the optical supermodes. The steady-state solution to (S8) is given by

$$\tilde{b}_{(m,\pm)} = (\mp)^m \frac{\kappa s_1 \sqrt{\gamma_1 \eta_c}}{2\xi [i\Delta_{(m,\pm)} - \bar{\gamma}/2]}, \text{ for } m = 1, 2. \quad (\text{S9})$$

The driving laser excites directly only the mode a_1^{cw} , therefore the steady state optical field transmitted through the bus waveguide is given by,

$$s_1^{out}(\omega_l) = s_1 - \sqrt{\gamma_1 \eta_c} a_1^{cw} \quad (\text{S10})$$

where the optical field $a_1(\omega_l)$ is given by Eq. (S7). The normalized field transmission, $t(\omega) = s_1^{out}(\omega)/s_1$ is given by,

$$t = 1 - i \frac{\gamma_1 \eta_c \kappa}{2\xi^2} \sum_{j=1,2} \left(\frac{\xi + i\alpha\kappa}{(-1)^j \beta + \xi + 2\bar{\Delta} + i\bar{\gamma}} + \frac{(-1)^j \kappa}{(-1)^j \beta - \xi + 2\bar{\Delta} + i\bar{\gamma}} \right), \quad (\text{S11})$$

where $\bar{\Delta} = \omega_l - \bar{\omega}$ is the detuning from the average frequency of the two cavities. The normalized power transmission is obtained from the relation $T(\omega) = |t(\omega)|^2$. In Fig. S4 we show the transmission $T(\omega)$ using the best-fit parameters $\bar{\omega}/(2\pi) = 188.442$ THz, $\bar{\gamma}/2\pi = 299$ MHz, $(\kappa, \beta)/2\pi = (1700, 298)$ MHz, and $\eta_c = 0.65$. The fit loaded optical quality factor is $Q = \bar{\omega}/\bar{\gamma} = 630,000$. To obtain the thermal tuned transmission of our device, we use Eq. (S11) together with the results described in section S2 B. The resonant frequency of the cavities, when the top-illumination is on, is given by is given by $\omega_m(T) = \omega_{m_0} + g_{th}\Delta T$, where $g_{th}/2\pi \approx -256$ MHz/K (see section S2 B).

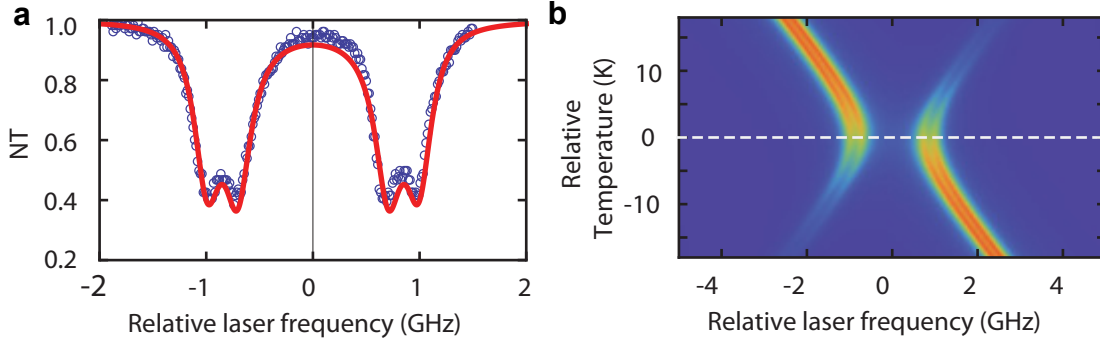


FIG. S4: **Optical transmission.** (a) Best-fit steady-state normalized optical transmission (red-line), calculated using equation (S11), and measured transmission spectrum (blue circles). The fit parameters are described in the text. (b) Optical transmission showing the thermal tuning of the coupled cavities, the false-color scale indicates the transmission. This map is obtained from (S11) using $\omega_1(T) = \omega_{1_0} + g_{th}\Delta T$, in good agreement with Fig. 2 in the main text.

C. Intrinsic mechanical frequencies

Using the optical read-out of the mechanical motion, as described in section S3 E, we measured the mechanical quality factors using a low power optical probe coupled to the lower frequency optical supermodel (right peak in Fig. S4a). The RF spectrum (100 averages) showing the two mechanical modes is shown in Fig. S5. The fit parameters are the mechanical frequencies and quality factors: $(f_L, f_R) = (50.283, 50.219)$ MHz and $(Q_{m_L}, Q_{m_R}) = (3.4 \pm 0.3, 2.3 \pm 0.2) \times 10^3$. Note that these intrinsic frequencies are slightly lower than the OMO self-sustaining oscillation frequency. This is due to the optical spring effect explained in the main text.

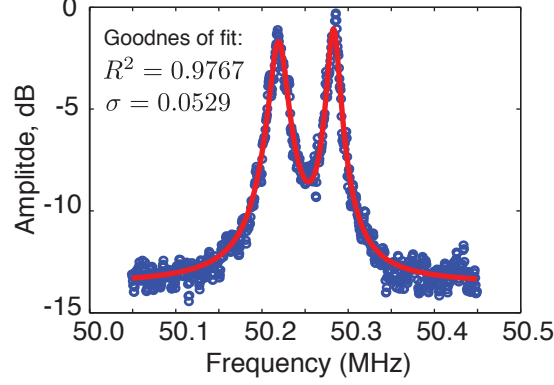


FIG. S5: **Mechanical modes RF spectrum.** (a) Double-Lorentzian best-fit steady-state normalized RF spectrum (red-line), and measured RF spectrum (blue circles). The fit parameters are described in the text.

D. Mechanical equations and optomechanical coupling

The mechanical degrees of freedom of each cavity x_1, x_2 follows the usual optomechanical equations^{20,24,40,41},

$$\ddot{x}_1 = -\Gamma_1 \dot{x}_1 - \Omega_1^2 x_1 + \frac{g_{om}}{m_{eff}^{(1)} \omega_0} \left(|a_1^{cw}|^2 + |a_2^{ccw}|^2 \right) + F_1^T(t), \quad (\text{S12a})$$

$$\ddot{x}_2 = -\Gamma_2 \dot{x}_2 - \Omega_2^2 x_2 + \frac{g_{om}}{m_{eff}^{(2)} \omega_0} \left(|a_1^{cw}|^2 + |a_2^{ccw}|^2 \right) + F_2^T(t), \quad (\text{S12b})$$

where $\Omega_i, \Gamma_i, m_{eff}^{(i)}$ represent the mechanical resonant frequency, dissipation rate, and effective motional mass. $F_T(t)$ is the thermal Langevin random force with expectation value $\langle F_i^T \rangle = 0$ and correlation function $\langle F_i^T(t) F_i^T(t + \tau) \rangle = 2k_B T m_{eff}^{(i)} \Gamma_i \delta(\tau)$, where k_B is the Boltzmann constant and $\delta(\tau)$ is the Dirac delta function. In contrast to the phonon-laser regime²⁵, we ignore terms which couples, through the mechanical displacement field, the optical modes $b_{(\pm,1)}$ with $b_{(\pm,2)}$; this is justified because $\kappa \gg \Omega_{L,R}$. Here we used the optical force as the positive gradient of the energy, this is a convention but must be consistent with whether the cavity frequency increases or decreases with increasing mechanical displacement; in our case the optical frequency decreases with the mechanical displacement⁷.

The full optomechanical dynamics is obtained by solving simultaneously Eqs. (S12) and (S5), such dynamics is discussed in detail in section S5. It is however instructive to analyze how a prescribed mechanical motion of the two mechanical oscillators is read-out through the optical modes (see section S3E), also how the optical force term in Eqs. (S12) couples to the two of them (see section).

E. Optical transduction of mechanical oscillations

To account for the mechanical effect on the optical transmission we first assume that the mechanical motion is independent of the optical fields¹⁶, which is equivalent to ignoring the dynamical back-action. Therefore we can use Eqs. (S6) for the optical eigenvectors and simply replace the optical cavity's resonant frequency by $\omega_i \rightarrow \omega_i + g_{om} x_i$, where x_i is the mechanical displacement amplitude for each cavity. The resonant frequency of each eigenmode $b_{(m,\pm)}$ will be given by,

$$\omega_{(1,\pm)}(x_i, x_j) = \bar{\omega}(x_i, x_j) \pm \xi(x_i, x_j)/2 \pm \beta/2, \quad (\text{S13a})$$

$$\omega_{(2,\pm)}(x_i, x_j) = \bar{\omega}(x_i, x_j) \pm \xi(x_i, x_j)/2 \pm \beta/2, \quad (\text{S13b})$$

where $\bar{\omega}(x_i, x_j) = [\omega_i(x_i) + \omega_j(x_j)]/2$, $\xi(x_i, x_j) = \kappa \sqrt{(1 - [\delta(x_i, x_j)/\kappa]^2)}$ and $\delta(x_i, x_j) = (\gamma_i - \gamma_j)/2 + [\omega_j(x_j) - \omega_i(x_i)]$. Due to the nonlinear $\xi(x_i, x_j)$ dependence on the mechanical displacement amplitudes $x_{1,2}$, The usual analytical approach to derive the optomechanical transduction coefficient does not apply¹⁶. However we can get insight into the problem if we consider the strong optical coupling limit, i.e., $\delta(x_i, x_j)/\kappa = g_{om}(x_i - x_j)/\kappa \ll 1$ which means that the optical frequency splitting

between the cavities is large compared to the mechanically induced frequency shift, therefore $\xi(x_i, x_j) \approx \kappa + \mathcal{O}(\delta^2/\kappa^2)$. To further simplify the analysis we assume that the two cavities share identical optical properties, i.e., $\omega_1(x_1 = 0) = \omega_2(x_2 = 0) = \omega_0$ and $\gamma_1 = \gamma_2 = \gamma_0$. In this case Eq. (S13) is approximated by,

$$\omega_{(m,\pm)}(x_1, x_2) \approx \omega_{0(m,\pm)} + g_{om}(x_1 + x_2) \quad (\text{S14})$$

where $\omega_{0(m,\pm)} = \omega_0 + (-1)^{m+1}\kappa/2 \pm \beta/2$. Combined with the above relations, Eq. S6 yields the following equation for the optical eigenmodes $b_{(m,\pm)}$,

$$\dot{b}_{(m,\pm)} = [-i\omega_{0(m,\pm)} - ig_{om}(x_1 + x_2) - \bar{\gamma}/2] b_{(m,\pm)}(\pm)^m \frac{\sqrt{\gamma_1\eta_{c1}}s_1 e^{i\omega t}}{2}, \text{ for } i=1,2. \quad (\text{S15})$$

The equations above (S15) can be formally integrated for a prescribed mechanical motion ($x_i = A_i \sin(\Omega_i t + \phi_i)$). The homogeneous solutions ($s_1 = 0$) decay exponentially and does not contribute after the initial transients. To find a particular solution satisfying (S15) we employ a common approach relying on the Jacobi-Anger expansion^{16,27},

$$\exp[i\mu_1 \cos(\Omega_1 t + \phi_1) + i\mu_2 \cos(\Omega_2 t + \phi_2)] = \sum_{p,q=-\infty}^{\infty} i^{p+q} J_p(\mu_1) J_q(\mu_2) e^{i(p\Omega_1 + q\Omega_2)t + i(\phi_1 + \phi_2)}, \quad (\text{S16})$$

where $\mu_i = g_{om}A_i/\Omega_i$ is the optomechanical modulation depth. Inserting Eq. (S16) in (S15) and solving the resulting equations gives,

$$b_{(m,\pm)}(t) = \frac{(\pm)^m s_1 \sqrt{\gamma_1\eta_{c1}}}{2} e^{i[\omega t + \sum_{j=1,2} \mu_j \cos(\Omega_j t + \phi_j)]} \sum_{p,q} \frac{i^{p+q} J_p(\mu_1) J_q(\mu_2) e^{i(p\Omega_1 + q\Omega_2)t}}{\bar{\gamma}/2 + i(-\Delta_{0(m,\pm)} + p\Omega_1 + q\Omega_2)}, \quad (\text{S17})$$

where the sum over m, n extends over $[-\infty, \infty]$, and $\Delta_{0(m,\pm)} = \omega_l - \omega_{0(m,\pm)}$. From Eq. (S17) we can clearly see that the cavity field exhibit tones at combinations of the mechanical frequencies ($m\Omega_1 + n\Omega_2$) of the two cavities.

S4. TOY MODEL FOR SYNCHRONIZATION

In this section we derive an approximate model to describe the essential features of our coupled oscillators. Although we develop a first order linear approximation of the two coupled optomechanical oscillators, **they constitute an intrinsically a nonlinear system**, as described in detail elsewhere²⁷.

A. Optically mediated mechanical coupling

The optical force driving terms in Eqs. (S12) can be written in terms of the diagonal modes $b_{(m,\pm)}$ from Eq. (S17) by using Eqs. (S7). As in section S3 E, for large optical coupling the terms are only resonant with the driving laser one at a time, therefore we can focus on the effect of a particular choice of (m, \pm) . To simplify the notation we use $\Delta_{0(m,\pm)} \equiv \Delta_m$ and $b_{(m,\pm)} \equiv b_m$ below. We also assume that effective motional mass of the individual oscillators are identical, i.e. $m_{\text{eff}}^{(j)} = m_{\text{eff}}$. The driving force in each oscillator is proportional to $|b_m|^2$,

$$F_{\text{opt}}^{(j)} = \frac{g_{om}}{\omega_{0(m)}} |b_m|^2 = -\frac{g_{om} P_{in} \gamma_1 \eta_{c1}}{4\omega_{0(m)}} \left| \sum_{p,q} \frac{i^{p+q} J_p(\mu_1) J_q(\mu_2) e^{i(p\Omega_1 + q\Omega_2)t}}{\bar{\gamma}/2 + i(-\Delta_m + p\Omega_1 + q\Omega_2)} \right|^2, \quad (\text{S18})$$

which contains both DC terms and oscillatory terms.

Although our oscillators may exhibit large oscillation amplitude ($g_{om}x_j > \bar{\gamma}$), it is instructive to analyze the small amplitude dynamics arising for the the driving term in Eq. (S18). This treatment is entirely analogous to the one used to derive the optomechanical damping and spring effect in uncoupled OMO's^{20,41}. For the small amplitude oscillation, the modulation parameters are small, i.e., $\mu_i = g_{om}x_i/\Omega_i \ll 1$, therefore the Bessel functions in (S18) can be approximated by their small argument limit, $J_n(\mu) \approx \frac{1}{n!}(\frac{\mu}{2})^n$. We neglect any terms which are quadratic in the $\mu_{1,2}$, which also account for summing Eq. (S18) only over $p, q = 0, \pm 1$ since higher order terms will result in terms which are $\mathcal{O}(\mu^2)$. The $p, q = 0$ terms result in a DC component of the force,

$$F_{\text{opt}_{DC}}^{(j)} = \sum_{j=L,R} \frac{g_{om}}{\omega_{0(m)}} \left(\frac{P_{in} \gamma_1 \eta_{c1}}{\Delta_m^2 + (\bar{\gamma}/2)^2} \right). \quad (\text{S19})$$

The impact of the DC term above is to shift the static equilibrium position of the mechanical oscillators. As a result, the actual optical detuning is also shifted, to account for this DC shift we substitute $\Delta_m \rightarrow \Delta'_m$, where $\Delta'_m = \Delta_m + g_{\text{om}}(x_1 + x_2)$.

When $p, q = \pm 1$ the resulting terms are quadratic in $\mu_{1,2}$ and **will be neglected in this first order approximation**, therefore the lowest order AC terms are given by combinations $(p, q) = (0, \pm 1)$ and $(p, q) = (\pm 1, 0)$.

$$F_{\text{optAC}}^{(j)} = \frac{g_{\text{om}}^2 P_{\text{in}} \gamma_1 \eta_{c1}}{\omega_{0(m)}} \sum_{j=L,R} A_j [-\cos(\Omega_j t) f_I(\Delta'_m, \Omega_j) + \sin(\Omega_j t) f_Q(\Delta'_m, \Omega_j)] \quad (\text{S20})$$

where the functions $f_{I,Q}(\Delta)$, which correspond to the in-phase ($\propto \sin(\Omega_j t)$) and quadrature of phase component ($\propto \cos(\Omega_j t)$) of the AC force, are given by

$$f_Q(\Delta'_m, \Omega_j) = \frac{4(\frac{\bar{\gamma}}{2})\Delta'_m}{2\Omega_j^2 \left((\frac{\bar{\gamma}}{2})^4 - \Delta_m'^4 \right) + \Omega_j^4 \left((\frac{\bar{\gamma}}{2})^2 + \Delta_m'^2 \right) + \left((\frac{\bar{\gamma}}{2})^2 + \Delta_m'^2 \right)^3}, \quad (\text{S21a})$$

$$f_I(\Delta'_m, \Omega_j) = \frac{2\Delta'_m \left((\frac{\bar{\gamma}}{2})^2 + \Delta_m'^2 - \Omega_j^2 \right)}{2\Omega_j^2 \left((\frac{\bar{\gamma}}{2})^4 - \Delta_m'^4 \right) + \Omega_j^4 \left((\frac{\bar{\gamma}}{2})^2 + \Delta_m'^2 \right) + \left((\frac{\bar{\gamma}}{2})^2 + \Delta_m'^2 \right)^3}. \quad (\text{S21b})$$

We can now use the transformations $\sin(\Omega_j t) \rightarrow x_j/A_j$, $\cos(\Omega_j t) \rightarrow \dot{x}_j/(A_j\Omega_j)$ and rewrite (S20) as

$$F_{\text{optAC}}^{(j)} = \frac{g_{\text{om}}^2 P_{\text{in}} \gamma_1 \eta_{c1}}{\omega_{0(m)}} \sum_{j=L,R} \left[-x_j f_I(\Delta'_m, \Omega_j) + \frac{\dot{x}_j}{\Omega_j} f_Q(\Delta'_m, \Omega_j) \right] \quad (\text{S22})$$

Equation (S22) above shows that for each oscillator the driving force will have a component proportional to its displacement (x_j) and its velocity (\dot{x}_j). But there are also terms proportional to the displacement and velocity of the opposing OMO; these are the terms that couple the two OMOs and form the basis for synchronization in our system. **Note that if higher order terms were kept in the expansion of Eq. (S18), nonlinear terms would appear in Eq. (S22).**

Above we derived the small amplitude form of the optical forces driving our coupled oscillators, we did not use the fact that our cavities are in the so-called unresolved sideband regime where the mechanical frequencies are much smaller than the optical linewidth, i.e., $\Omega_j/\bar{\gamma} \approx 0.2 \ll 1$. In this limit, Eqs. (S23) can be written as,

$$f_Q(\Delta'_m) \approx \frac{4(\frac{\bar{\gamma}}{2})\Delta'_m}{\left((\frac{\bar{\gamma}}{2})^2 + (\Delta'_m)^2 \right)^3}, \quad (\text{S23a})$$

$$f_I(\Delta'_m) \approx \frac{2\Delta'_m}{\left((\frac{\bar{\gamma}}{2})^2 + (\Delta'_m)^2 \right)^2}. \quad (\text{S23b})$$

Now we can write the (S12) as two coupled harmonic oscillators,

$$\ddot{x}_1 + \Gamma'_1 \dot{x}_1 + (\Omega'_1)^2 x_1 = -k_1 x_2 + k_Q \dot{x}_2, \quad (\text{S24a})$$

$$\ddot{x}_2 + \Gamma'_2 \dot{x}_2 + (\Omega'_2)^2 x_2 = -k_1 x_1 + k_Q \dot{x}_1, \quad (\text{S24b})$$

where the modified frequency and damping rate are given by (assuming $\delta\Omega_j^2 \approx 2\Omega_j\delta\Omega_j$),

$$\Gamma'_j = \Gamma_j - \beta_j f_Q(\Delta'_m), \quad (\text{S25a})$$

$$\Omega'_j = \Omega_j + \frac{\beta_j}{2} f_I(\Delta'_m), \quad (\text{S25b})$$

$$k_Q^{(j)} = \beta_j \Omega_j f_Q(\Delta'_m), \quad (\text{S25c})$$

$$k_I^{(j)} = \beta_j \Omega_j f_I(\Delta'_m) \quad (\text{S25d})$$

with $\beta_j = g_{\text{om}}^2 P_{\text{in}} \gamma_1 \eta_{c1} / (m_{\text{eff}}^j \omega_{0(m)} \Omega_j)$.

Therefore, in the small modulation regime ($\mu_{1,2} \ll 1$), our system resemble harmonic oscillators in which both the damping and frequency are controlled by the optical field; this result is exactly what one would get from uncoupled OMOs. With the reduction of the mechanical damping rate for a blue detuned laser. ($\Delta'_m > 0$), these two damped oscillators may undergo a bifurcation when the effective damping rate (Γ'_j) reverses sign. In this first order approximation there is no additional nonlinearity to prevent the oscillations to grow unbound, however it is known that the higher order terms in the force expansion ((S18)) will balance the amplitude growth and eventually lead to a stable periodic orbit (limit cycle)^{15,16,27}. The optical coupling in our system couples the two harmonic oscillators with both amplitude and velocity dependent terms, with coupling strengths k_I, k_Q , respectively. The functional dependence of such coupling is the same as the self-induced optical spring and damping rate, as given by (S25).

B. Approximate Kuramoto model

In the small amplitude approximation that lead to Eq. (S24), one can also derive slowly-varying phase and amplitude equations that describe the dynamics of our system. To accomplish this we assume the following form for our displacement amplitudes,

$$x_1(t) = r_1(\tau) \exp i\phi_1(\tau) \exp i\Omega t, \quad (\text{S26a})$$

$$x_2(t) = r_2(\tau) \exp i\phi_2(\tau) \exp i\Omega t. \quad (\text{S26b})$$

where $\Omega = (\Omega_1 + \Omega_2)/2$ is the average frequency of oscillation. Substituting this ansatz in Eqs. (S24) and assuming that the negative damping induced by the optical wave exactly balances the intrinsic viscosity of the oscillators ($\Gamma' \approx 0$) we obtain the following amplitude and phase equations,

$$\dot{r}_1 = -\frac{k_Q r_2}{4\Omega^3} ((\Omega^2 + \Omega_2^2) \cos(\Delta\phi)) - \frac{k_I r_2 \sin(\Delta\phi)}{2\Omega}, \quad (\text{S27a})$$

$$\dot{r}_2 = -\frac{k_Q r_1}{4\Omega^3} ((\Omega^2 + \Omega_1^2) \cos(\Delta\phi)) + \frac{k_I r_1 \sin(\Delta\phi)}{2\Omega}, \quad (\text{S27b})$$

$$\dot{\Delta\phi} = 2\Delta\Omega + \frac{(R^2 - 1) \cos(\Delta\phi) (\gamma k_Q + 2k_I)}{2R\Omega} + \frac{(R^2 + 1) \sin(\Delta\phi) k_Q}{R} \quad (\text{S27c})$$

where $\Delta\phi = \phi_1 - \phi_2$, $R = r_1/r_2$ and $\Delta\Omega = \Omega'_1 - \Omega'_2$. Note that in this approximation the limit cycle has zero amplitude; this is the case because we neglected the higher order terms when deriving Eq. (S24). Despite such limitations of this toy model, the phase dynamics given by Eq. (S27) enables us to visualize how does the Arnold tongue ($|\Delta\Omega| < k_I$) behaves as we vary the laser detuning. We assume that limit cycles of the individual oscillator will have similar amplitude ($R = 1$) and require $\dot{\Delta\phi} = 0$ for a synchronized oscillation. When $|\Delta\Omega| < k_I$ this conditions can be satisfied and defines an Arnold tongue for this simple model; inside the Arnold tongue the system can synchronize ($\dot{\Delta\phi} = 0$). In Fig. S6 we show the Arnold tongue plot for our system, in Fig. S6a we plot it in the usual way, as function of the coupling coefficient (k_I), whereas in Fig. S6b we plot the tongue as a function of the laser detuning by using Eq. (S25). Due to the model simplicity and lack of higher order terms, it does not predict the precise values for the synchronization region observed in the experiment (Fig. S6b), however it does agree qualitatively; for higher optical power levels the tongues get wider and allows a given mechanical frequency difference to synchronize at larger detuning, as shown in figure 3 of the main text.

C. Oscillation treshold

The individual threshold to achieve self-sustaining optomechanical oscillations can be estimated by forcing $\Gamma' = 0$ in Eq. (S25), the resulting threshold condition ($\Delta' = \bar{\gamma}/2$) follows the expression,

$$P_{th} = \frac{\Omega_m m_{\text{eff}} \omega^4}{8\eta_c g_{\text{om}}^2 Q_m Q^3} \quad (\text{S28})$$

where Q is the optical quality factor, Q_m is the mechanical quality factor, $\eta_c = \gamma_e/\gamma$ is the ideality coupling factor, it can be obtained from the experimental spectrum through its relation to the minimum transmission value³⁹. In our experiment $\eta_c = 0.65$ (see Fig. S4). Since the threshold depends nonlinearly on several measured and calculated parameters we propagate the error through the usual relation,

$$\frac{\delta P_{th}}{P_{th}} = \sqrt{\left(\frac{\delta m_{\text{eff}}}{m_{\text{eff}}}\right)^2 + \left(\frac{\delta \Omega_m}{\Omega_m}\right)^2 + \left(4\frac{\delta \omega}{\omega}\right)^2 + \left(2\frac{\delta g_{\text{om}}}{g_{\text{om}}}\right)^2 + \left(3\frac{\delta Q}{Q}\right)^2 + \left(\frac{\delta Q_m}{Q_m}\right)^2} \quad (\text{S29})$$

where the δ before each quantity indicates its standard deviation. The sum of relative errors is dominated by the errors bars of g_{om} and Q , using the error bars indicated in the main text we obtain $\delta P_{th}/P_{th} \approx 35\%$. This is a large deviation but is found to impact only the precise optical input power that results in a RF spectral map that matches the experimental data, as shown in the main text.

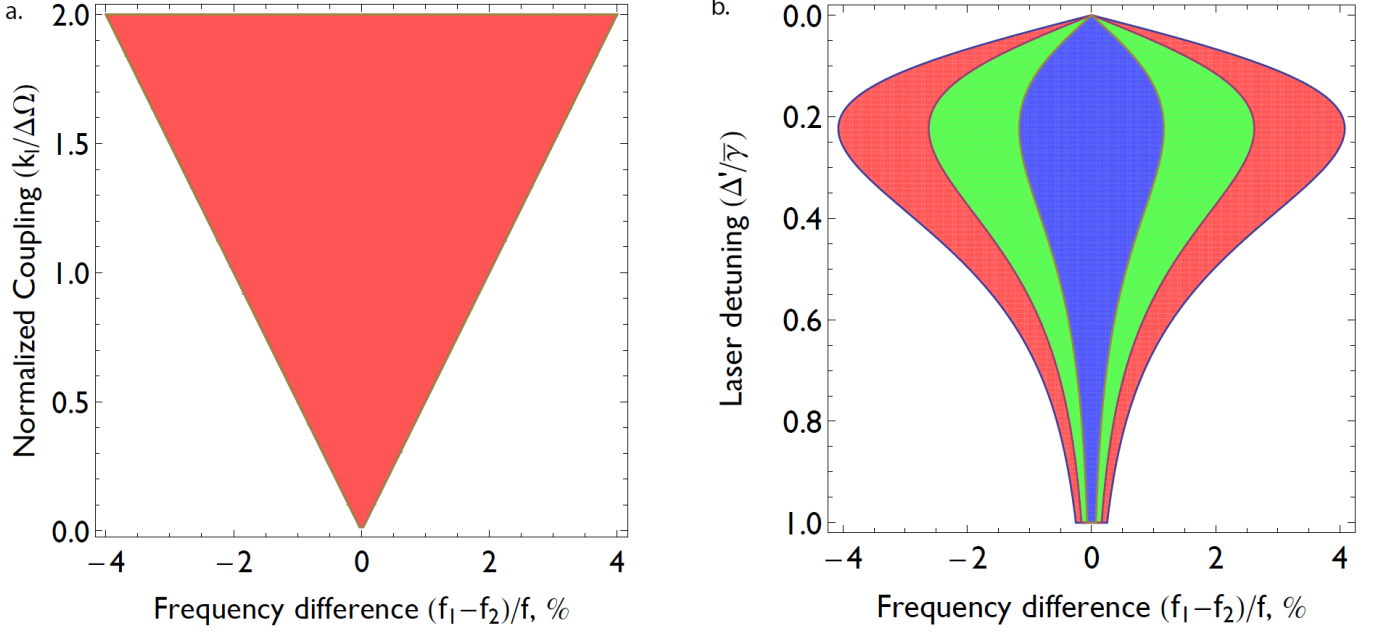


FIG. S6: Arnold tongue for the simplified Kuramoto model, inside the tongues the system can exhibit synchronized oscillation. (a) Usual tongue as a function of the coupling parameter k_l . (b) Tongue when k_l is explicitly written in terms of the laser-cavity detuning. The three tongues in (b) are obtained with the optical input power values of $P_{in} = 1, 5, 15 \mu\text{W}$, the lower power is the blue whereas the highest power is red tongue. f is the average mechanical frequency of the oscillators.

S5. SYNCHRONIZATION SIMULATION

A. Simulation approach

To simulate the synchronization dynamics and obtain the results shown in Fig. S7, we numerically integrate the system of equations (S5), including the displacement dependent optical resonant frequencies, i.e. $\omega_{1,2}(x) = \omega_{1,2} + g_{om}x_{1,2}$, together with the two harmonic oscillator equations (S12). This is accomplished using the *NDSolve* function in the commercial software Mathematica®. In the absence of the random thermal noise force in Eq. (S12), it is numerically challenging to capture the dynamics before the regenerative oscillation threshold is reached, this is because the steady-state is a static one, i.e., $\dot{x}_{1,2} = 0$. To overcome this issue we add a weak (low-temperature $T = 1 \text{ K}$) noise that prevents the dynamics to reach such static equilibrium. Since *NDSolve* is a deterministic solver we include the thermal drive by assigning to $F_{1,2}^T(t)$ the outcome of a random variable with with expectation value and correlation function given by

$$\langle F_i^T \rangle = 0 \quad (\text{S30})$$

$$\langle F_i^T(t) F_i^T(t + \tau) \rangle = 2k_B T m_{eff}^{(i)} \Gamma_i \delta(\tau), \quad (\text{S31})$$

where k_B is the Boltzmann constant. The discontinuity of this random driving term can lead to instabilities in *NDSolve*, to overcome this we smooth out the noise term by interpolating the random force with a correlation time $t_c = (2\pi/\Omega_i)/30$. Such short correlation time ensures that the noise power spectrum density (PSD) is white within the frequency range of interest. The reliability of this approach is confirmed by verifying that for weak pump powers ($P \ll P_{th}$), the integrated power spectrum density $S_{x_i}(\Omega) = |x_i(\Omega)|^2$ satisfy the fluctuation-dissipation theorem⁴².

$$\langle x^2(\Omega) \rangle = \frac{1}{2\pi} \int_0^\infty S_{xx}(\Omega) d\Omega = \frac{k_B T}{2m_{eff}^{(i)} \Omega_i^2} \quad (\text{S32})$$

A complete analysis of the noise in synchronized systems is beyond the scope of this work, since an accurate numerical noise dynamics will require the simulation of the coupled non-linear stochastic dynamics of the optomechanical cavities^{43,44}. The computational complexity of such systems is also high due to the requirement for slow convergence, first order, fixed time step simulation⁴⁵⁻⁴⁷.

B. Simulation results

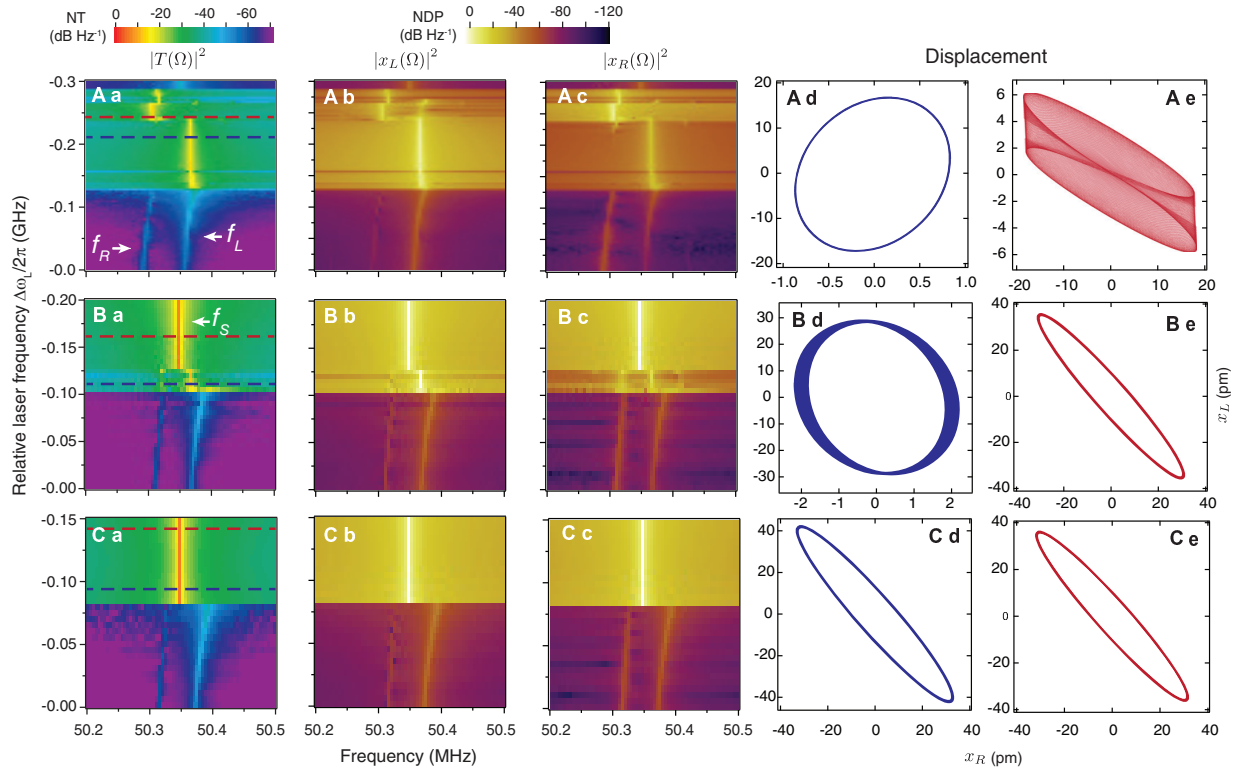


FIG. S7: **Numerical simulation of the coupled oscillation dynamics.** From **a** to **e**: transmission RF spectra, displacement power RF spectra of the L and the R OMOs, and the displacement phase diagram of the L and the R OMOs, for input powers at (A) $P_{in} = 4.9 \mu\text{W}$, (B) $P_{in} = 15.8 \mu\text{W}$ and (C) $P_{in} = 17.9 \mu\text{W}$. x_L (x_R): displacement of the L and R OMOs.

The simulation also allows us to probe not only the optical transmission PSD, but also the mechanical displacement PSD and time series of each OMO. The complete simulation results for the pump laser powers described in the main text are shown in fig. S7. The only parameter we adjusted to obtain the maps shown in figures 3 (f,g,h) in the main text and S7 was the optical pump power.

In figures S7A ($P_{in} = 4.9 \mu\text{W}$), the mechanical power spectrum of the oscillators (fig. S7A(b,c)) shows that for $(-0.25 < \Delta\omega/2\pi < -0.13 \text{ GHz})$, only L OMO is oscillating; the R OMO is forced to oscillate at the L OMO's frequency but has not yet reached its oscillation threshold. This is illustrated by the displacement state space figures shown in fig. S7A(e) for $\Delta\omega/2\pi = -0.21 \text{ GHz}$ (blue dashed line in fig. S7A(a)), note that $|x_L|$ is about 20 times larger than $|x_R|$. At $\Delta\omega/2\pi = -0.25 \text{ GHz}$, marked by the red-dashed line in fig. S7A(a), the situation changes and the R OMO oscillates with larger amplitude ($|x_R| \approx 3.5|x_L|$) but at different frequencies; the result is a Lissajous figure that fills the whole state space.

In figures S7B ($P_{in} = 15.8 \mu\text{W}$), in the asynchronous region, indicated by the blue dashed line, the L OMO oscillates with an amplitude roughly 15 times of the R OMO in agreement with the measured RF spectrum and the pump probe measurement. In the unified frequency region, for both power levels $P_{in} = 15.8 \mu\text{W}$ and $P_{in} = 17.9 \mu\text{W}$ in fig. S7C, the phase diagram shows the two oscillators are synchronized and their amplitude differ less than 20% in agreement to the pump-probe measurements. The synchronization phase for figs. S7C(d-e) is roughly $\phi = 160^\circ$, also all the simulations for our system resulted in phase differences close to π , in agreement with the discussion in²⁷ that the anti-phase synchronization is a more stable state when the oscillations amplitude x_L, x_R are not identical.

The criteria for the optimum fitting is the matching of the laser frequency at which the bifurcation occurs, which is sufficient for explaining all of the non-linear phenomena observed. The difference in the simulation power level and experimentally measured power level may be due to the variations in etched geometry, film thickness and optical losses. Fitting the entire spectra may provide a closer numerical match but it requires a full analysis taking account of non-linear error propagation, detector and spectrum analyzer response function and multidimensional fitting that is beyond the scope of this paper.